PAPER

Check for updates

Electrochemical performance of Cu₆Sn₅ alloy anode materials for lithium-ion batteries fabricated by controlled electrodeposition†

Minyue Wen,[a] Jiafu Yu,[a] Jiawen Wang,[a] Shuaihao Li[a] and Qiuyu Zeng [ID] *[b]

Combining electrodeposition and heat treatment is an effective method to successfully fabricate Cu₆Sn₅ alloy materials, in which the S2 alloy electrode is electrodeposited at 1.2 A dm⁻² current density with uniform and compact morphology. The characterization results show that monoclinic η′-Cu₆Sn₅ and hexagonal η-Cu₆Sn₅ phases fabricated at the appropriate current density exhibit excellent electrochemical performance. The optimal Cu₆Sn₅ alloy anode material boasts not just a significantly high discharge specific capacity of 890.2 mA h g⁻¹ with an initial coulombic efficiency (ICE) of 73.96%, but also achieves an adequate discharge specific capacity of 287.1 after 50 cycles at 100 mA h g⁻¹. Moreover, the electrodeposited Cu₆Sn₅ alloy materials also possessed a lower transfer resistance of 42.45 Ω and an improved lithium-ion diffusion coefficient of 2.665×10^{-15} cm² s⁻¹ at the current density of 1.2 A dm⁻². Therefore, preparing the Cu₆Sn₅ alloy thin-film electrode could be a cost-effective and straightforward method by electrodeposition from cyanide-free plating baths to develop anode components suitable for lithium-ion battery applications.

1 Introduction

To satisfy the rapidly increasing demands for higher energy density, stable electrochemical performance, and high safety of electrical devices, lithium-ion batteries (LIBs) are universally acknowledged as a favorable choice for energy storage.[1,2] The anode material plays a significant role in enhancing the battery performance, but the deployment of graphite-anode LIBs in commercial applications encounters substantial obstacles with a relatively modest theoretical specific capacity of only 372 mA h g⁻¹ as well as poor rate performance.[3–5] Consequently, the design and development of innovative anode materials that exhibit enhanced theoretical specific capacity are gaining increasing importance, in which Sn-based materials have garnered significant attention as potential candidates for further investigation due to their exceptional theoretical capacity of 993 mA h g⁻¹, appropriate working voltage, excellent electrical conductivity, and abundance in nature.[6] Nevertheless, the rapid capacity loss is a common issue for Sn-based materials due to significant volumetric variations during lithium insertion/extraction processes, which will bring about cracking

and pulverization of electrodes with drastic structural collapse and poor cycling stability.[7] As a result, some efficient strategies are implemented to overcome these shortcomings, such as constructing the Sn–M (M = Cu, Fe, Sb, Co, *etc.*) alloy composite structure, where M is an inactive element.[8–11] The inactive element can be used to create a conductive and ductile framework for containing the lithiated tin particles, which can withstand some of the damaging expansion/contraction of the Li$_x$Sn particles during discharge and charge.[12] Among traditional Sn alloy systems, the Sn–Cu alloy, specifically Cu₆Sn₅, which has a theoretical capacity of 605 mA h g⁻¹, has been viewed as a potential alternative anode material for LIBs because it can mitigate the peeling of electrodes and exhibit a lower oxidation potential, which have a positive impact on electrochemical performance.[13,14] It is noteworthy that the structural integrity of Cu₆Sn₅ is strong among the original Sn–Cu intermetallics and their lithium-inserted counterparts, while also providing cost-effective high energy storage.[15,16] Furthermore, many methods are employed to fabricate Cu₆Sn₅ alloys, such as electron beam evaporation deposition,[17] solution synthesis,[18,19] and electrodeposition,[20,21] of which electrodeposition is an efficient method for achieving large-scale manufacturing of alloy electrodes due to its high productivity, simple process, and relative cost-effectiveness.

A facile strategy is proposed to ameliorate the intractable problem of restricted useable discharge capacity and unsatisfactory cycling durability of Sn–Cu alloy electrodes reported, which is mainly due to the diminished effective proportion of active elements and substantial volume fluctuations of alloy

[a]College of Chemistry and Environmental Engineering, Yangtze University, Jingzhou, 434023, P. R. China

[b]School of Material Science and Engineering, Anhui University of Science and Technology, Huainan 232000, China. E-mail: qiuyuzeng@foxmail.com; Tel: +86 15313251023

† Electronic supplementary information (ESI) available. See DOI: https://doi.org/10.1039/d4ra04562a

electrode substances.[20,22,23] Electrodeposition is a simplicity and efficient way to fabricate Cu_6Sn_5 alloy electrodes at various current densities from cyanide-free plating solution, which has the benefits of straightforwardness, productiveness, and controllability of the surface structure and grain size. Furthermore, the electrodeposition Cu_6Sn_5 at the appropriate current density can create a uniform and dense surface structure, which can facilitate substantial reduction in ion diffusion distances, thereby improving the cycling stability and rate capability of alloy electrodes. Therefore, Cu_6Sn_5 alloy particles are prepared from cyanide-free plating solution by electrodeposition at different current densities and controlled heat treatments to further improve the densification of Cu_6Sn_5 alloy nanoparticles in this work.

2 Experimental

2.1 Materials preparation

After being cut into 5.5 cm × 7.5 cm pieces, the copper foils as substrate are polished with sandpaper, repeatedly pressed with a roller press, and ultrasonically cleaned before use. To prepare the electroplating solution, 30.00 g of $K_4P_2O_7 \cdot 3H_2O$, 2.00 g of $C_6H_6O_2$, 1.25 g of KNO_3, and 0.10 g of hexadecyl trimethyl ammonium bromide are gradually introduced into 150.0 mL of deionized water, resulting in the formation of a transparent yellow solution. Then 2.25 g of $SnCl_2 \cdot 2H_2O$, 1.25 g of $CuSO_4 \cdot 5H_2O$, and 0.13 g of ethylenediamine are added into the yellow solution as illustrated in Fig. 1. Last, the final plating solution is made clear and transparent with the addition of deionized water and ammonia, in which the pH value is adjusted to 9. Cu_6Sn_5 anode materials are fabricated by electrodeposition at 1.0, 1.2, 1.5, and 1.7 A dm^{-2} lasting for 10 min, respectively, and then calcined in a muffle furnace at 200 °C for 10 h. The final calcined products which include monoclinic η'-Cu_6Sn_5 and hexagonal η-Cu_6Sn_5 phase are labeled S1, S2, S3, and S4, corresponding to the current density of 1.0, 1.2, 1.5, and 1.7 A dm^{-2}, respectively. The space group of monoclinic Cu_6Sn_5 is $C2/c$ (15) and the space group of hexagonal $Cu_{6.26}Sn_5$ is $P63/mmc$ (194). Analytical reagents are used in this experiment without any additional purification.

2.2 Performance characterization

X-ray diffraction (XRD, PALMERNACO) from 20 to 90° at a scan rate of 10° min^{-1} is employed to characterize the crystal structure of the obtained samples. The X-ray photoelectron spectroscopy (XPS, Thermo K-Alpha) is used to measure the chemical valence and chemical environment of the elements on the sample surface. The microstructure and elemental composition of the samples are examined using a field emission-scanning electron microscope (FE-SEM, MIRA3, TESCAN) equipped with an energy dispersive spectrometer (EDS, BRUKER). The fabricated Cu_6Sn_5 alloy electrodes are constructed into CR2025-type coin batteries, in which the copper foil can be punched into a 12 mm diameter disk directly as the working electrode, lithium metal serves as the counter electrode, and the electrolyte is 1.0 mol $LiPF_6$ in EC : DMC = 1 : 1 vol% with 10.0% FEC (Suzhou DuoDuo Chemical Technology Co., Ltd). The charge–discharge cycle stability of the coin cells is measured with an operating voltage range from 0.01 to 2.00 V *via* a battery test system (CT 2001A, Land) at 100 mA g^{-1}. A CHI660E electrochemistry workstation (Shanghai Chenhua Co., Ltd, China) is utilized for recording the voltage variations of cyclic voltammetry (CV) curves to explore the reaction mechanism of the electrodes from 0.01 V to 3.00 V. To compute the Li^+ diffusion coefficient, the same workstation is employed to record the electrochemical impedance spectroscopy (EIS) profiles with an amplitude of 5.00 mV from 10^5 to 10^{-2} Hz.
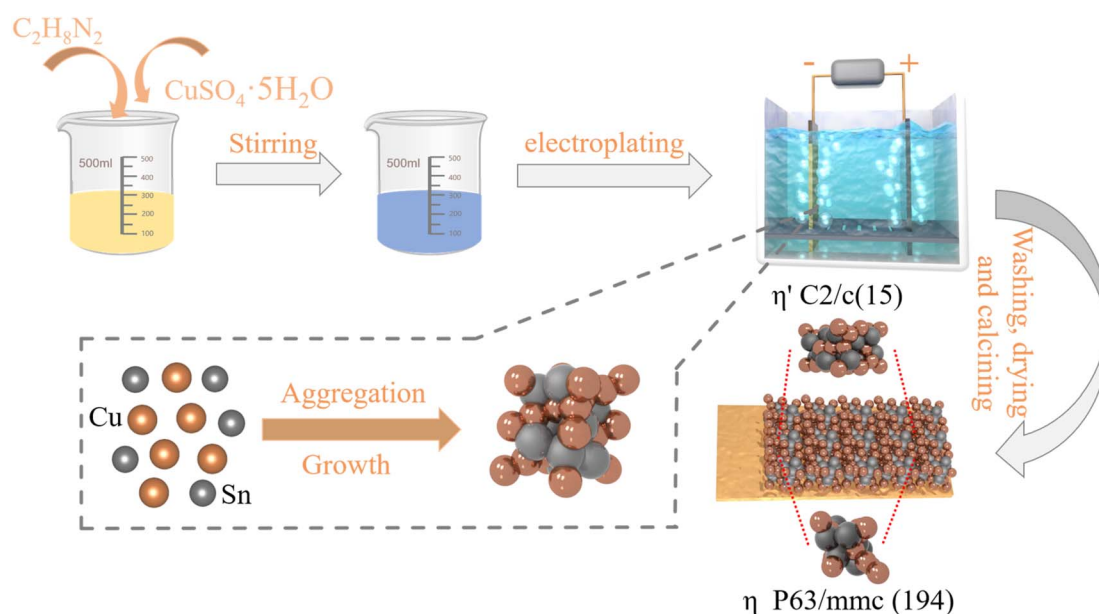

Fig. 1 Schematic diagram of the fabricated Cu_6Sn_5 alloy electrodes.

3 Results and discussion

XRD patterns are analyzed to identify the crystal structure of the as-fabricated samples and to measure the chemical valence and chemical atmosphere of the elements, XPS is employed in Fig. 2. Fig. 2(a) reveals that the four samples prepared at varying current densities all display distinctive diffraction peaks at 30.1°, 43.0°, and 43.3°, corresponding to the (101), (110), and (102) planes of $Cu_{6.26}Sn_5$ phase (JCPDS: NO. 47-1575) as well as the (22-1), (132), and (42-2) planes of Cu_6Sn_5 phase (JCPDS: NO. 45-1488). Moreover, the distinct peaks observed at 43.3°, 50.5°, and 74.1° are ascribed to the Cu foil substrate.[24] It is noteworthy that the diffraction peaks of Cu_3Sn are present in the XRD patterns of S3 and S4 samples, but the Cu_3Sn phase is virtually inactive against lithiation at room temperature.[25] Furthermore, the enlarged detail patterns of S1, S2, S3, and S4 samples near the 30.1° diffraction peak in the XRD pattern indicate that the varying current density may indeed lead to fine-tuning of the internal structure of the crystal. Fig. S1† depicts the comprehensive spectra of the prepared S2 sample, revealing that Cu and Sn elements are present in the surface layer, which is in accordance with the outcomes of EDS. As illustrated in Fig. 2(b), the Cu 2p XPS spectra with high resolution can be decomposed into two well-defined peaks, two peaks of 934.3 and 954.4 eV are

assigned to Cu $2p_{3/2}$ and Cu $2p_{1/2}$ of Cu^{2+}, and the peaks of 933.6 and 954.0 eV are ascribed to Cu $2p_{3/2}$ and Cu $2p_{1/2}$ of Cu^0, respectively. The two peaks at 942.4 and 962.2 eV can be identified as the satellite peaks of Cu 2p due to the unfilled $3d^9$ state. In Fig. 2(c), in the Sn 3d spectra, the peaks positioned at 486.8 eV and 495.2 eV are ascribed to Sn^{4+}, while the peaks situated at 484.7 eV and 493.3 eV are linked to Sn^0.

In Fig. 3, the SEM images depict the morphological characteristics of S1, S2, S3, and S4 electrodes fabricated at various current densities. The SEM image of S1 presents a loose spherical granular agglomerate structure with a sizeable gap between the grains and visible more defect holes on the surface of S1, as revealed in Fig. 3(a and e). The surface of sample S2 is dense as depicted in Fig. 3(b and f), in which the surface grains are small and the flatness is high. It's worth noting that as current density increases, the surface density decreases on the surfaces of S2, S3 and S4. Fig. 3(c and g) reveals that the grain growth on the surface of S3 is uniform, but the density remains lower compared to sample S2. Furthermore, as depicted in Fig. 3(d and h), the surface roughness of S4 increases and there are evident fluffy pores. This may be attributed to the too rapid crystallization, enhanced concentration polarization, and intensified hydrogen evolution, leading to many large-sized spherical crystal particles appearing on the surface of S4.
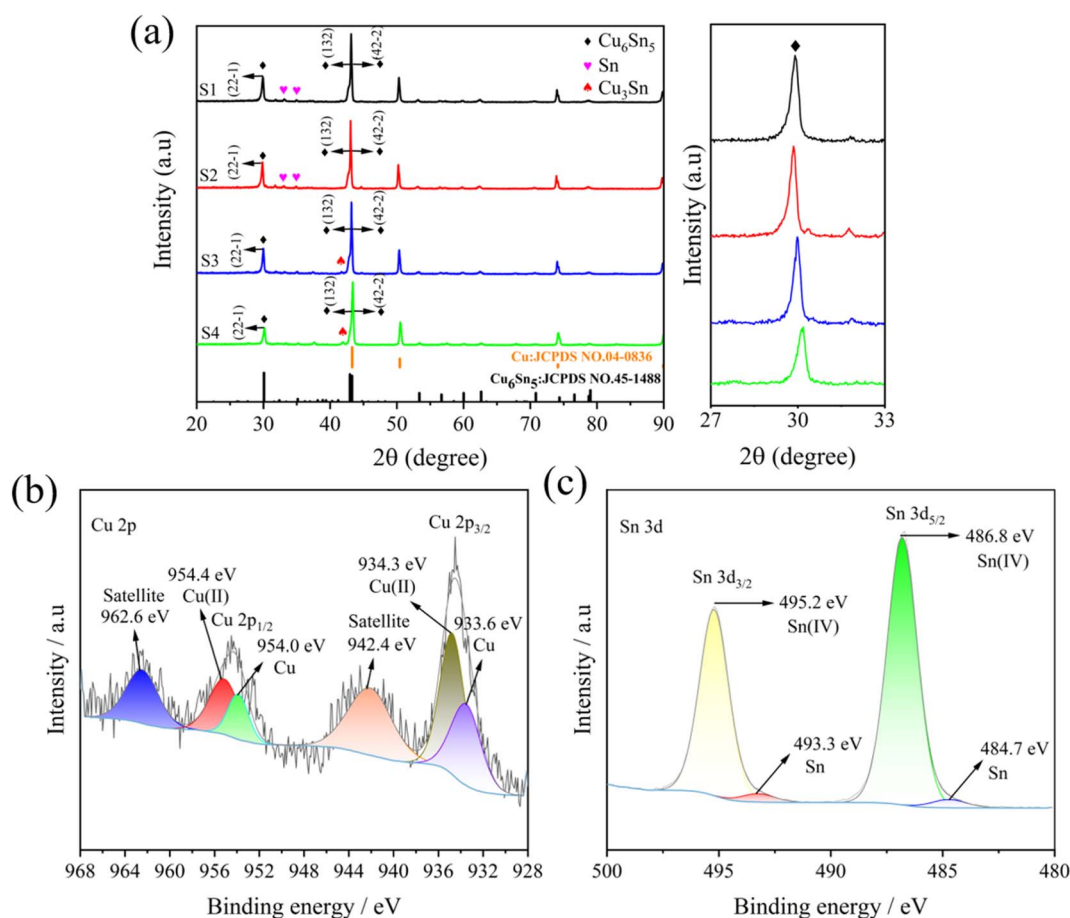

Fig. 2 XRD patterns (a) of S1, S2, S3, and S4 electrodes as well as their partial enlarged details; Cu 2p (b) and Sn 3d (c) spectra of the S2 sample.
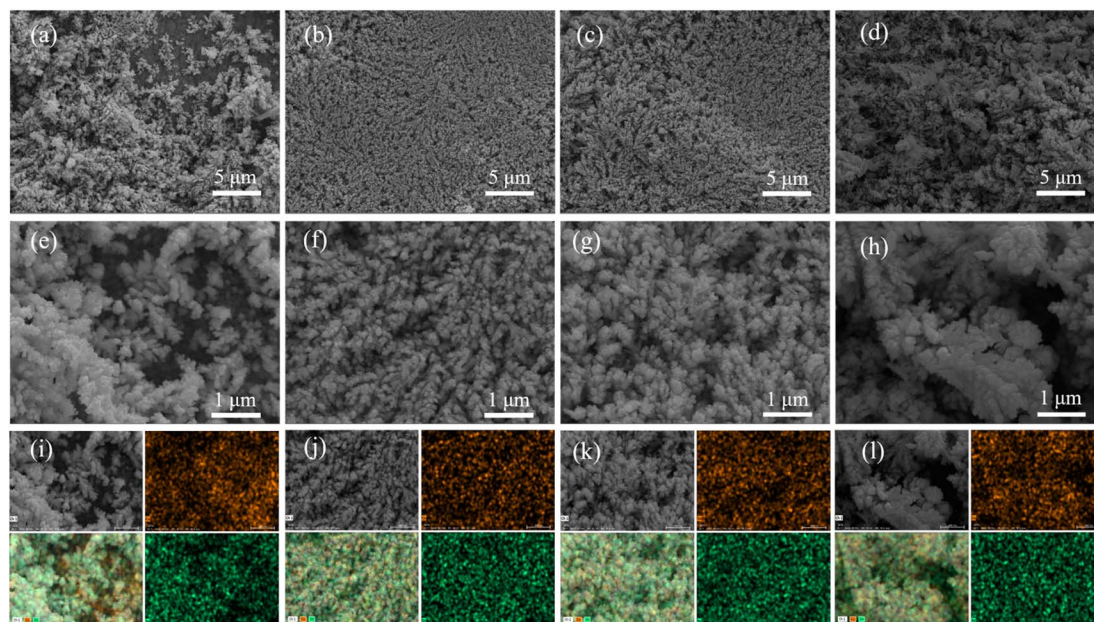
Fig. 3 SEM images of the fabricated S1 (a and e), S2 (b and f), S3 (c and g), and S4 (d and h); EDS mapping images of S1 (i), S2 (j), S3 (k), and S4 (l).

Fig. 3(i–l) shows the EDS mapping images corresponding to the S1, S2, S3, and S4 samples, indicating that all four samples contain copper and tin. Therefore, it can be inferred that S2 has a uniform and compact interface, which significantly enhances its electrochemical characteristics by strengthening the connection and reducing resistance at the electrode–current collector interface.

Galvanostatic charging–discharging tests are used to evaluate the electrochemical performance of the Cu_6Sn_5 alloy electrodes prepared by electrodeposition, as depicted in Fig. 4. Fig. 4(a) depicts the initial curves of galvanostatic charging and discharging, in which the S2 alloy electrode has an initial coulombic efficiency (ICE) of 73.96% and exhibits a remarkable discharge specific capacity of 890.2 mA h g^{-1}, while the coin cells with the S1, S3, and S4 alloy electrodes possess ICE values of 70.06%, 71.57%, and 79.06%, respectively. In Fig. 4(b), it is depicted that the cells that are assembled with the S1, S2, S3, and S4 electrodes exhibit cycling stability during 50 cycles at 100 mA g^{-1}. It's worth noting that the curves show that the S2 alloy electrode has superior charge–discharge performance compared to other electrodes. During the initial 26 cycles, the specific discharge capacity of the S2 alloy electrode exceeds that of the other three electrodes. The specific discharge capacity decreases quickly after 26 cycles, but it remains at 287.1 mA h g^{-1} after the 50th cycle. To verify the reliability of the results, error bars for the first discharge specific capacity and first cycle efficiency of the four samples are shown in Fig. S2.† To better understand the significance of this work, in Table 1, the comparison of Cu–Sn material battery performance in previous studies and the current work is shown. In this work, Cu_6Sn_5 has a superior electrochemical property, and a simple and affordable method is proposed to fabricate the Sn-based material directly through electrodeposition, in which the

current density can be adjusted to control the size and volume change of Cu_6Sn_5 particles. When considering the coulombic efficiency as depicted in Fig. 4(c), the four samples demonstrate steady performance with efficiencies exceeding 93% after the first cycle, revealing that these alloy anodes materials have favorable reversibility during the discharge/charge process. The rate cycling tests of the S2 electrode deposited at 1.2 A dm^{-2} are displayed in Fig. 4(d), in which the S2 electrode consistently exhibits high discharge specific capacities of 580.4, 487.9, 407.7, and 303.2 mA h g^{-1} at 100, 200, 500, and 1000 mA g^{-1}, respectively. In addition, when the current is suddenly adjusted to 100 mA g^{-1}, the discharge specific capacity of the S2 electrode can rapidly recover to 511.8 mA h g^{-1} with an exceptional coulombic efficiency, which indicates the structural stability of the S2 sample maintained during various cycling rates.

The CV curves and galvanostatic discharge and charge profiles are conducted to evaluate the electrochemical reaction mechanism of the S2 electrode in Fig. 5. Five reduction peaks can be observed at 1.23, 0.97, 0.53, 0.22, and 0.02 V during the initial cathodic scan as shown in Fig. 5(a). It is noteworthy that these distinctive peaks observed during the first cycle at 0.97 and 1.23 V correspond to the emergence of other irreversible reactions of some oxides and a solid electrolyte interphase (SEI) film.[31] A small amount of SEI film is still formed in each subsequent cycle, but it disappears in the fifth cycle.[32–34] Moreover, the reduction peaks about 0.22, 0.31 and 0.53 V signify the emergence of the intermediate $Li_xCu_6Sn_5$ alloy composition and subsequent embedding of Li$^+$ into $Li_2Cu_6Sn_5$ to form the Li_2CuSn compound according to eqn (1) and (2).[35,36] Evidently, the peak emerging at 0.02 V can be unequivocally linked to the $Li_{3.5}Sn$ alloy phase, in accordance with eqn (3), which corresponds to the lithium intercalation processes of Cu_6Sn_5 alloy as described in previous reported.[37] Considering
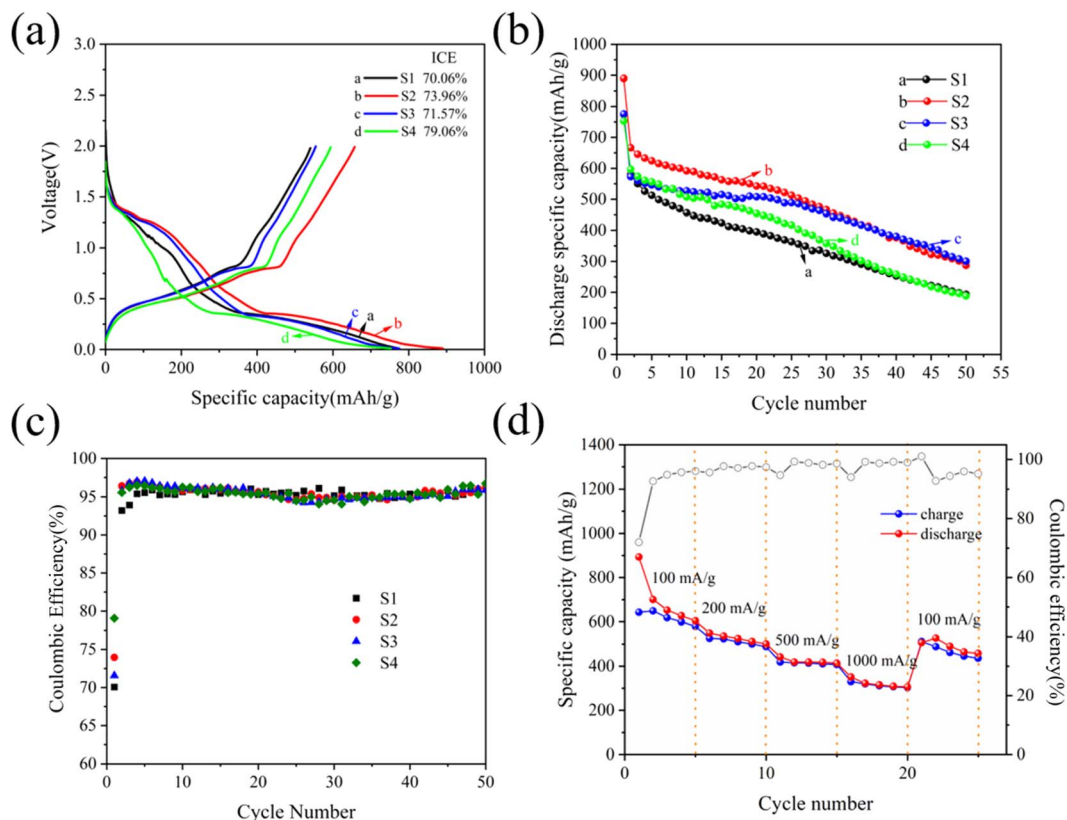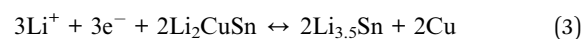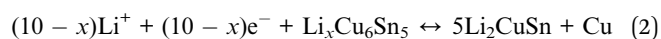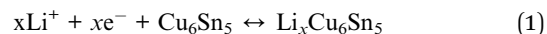
Fig. 4 Initial galvanostatic charge and discharge curves (a) and cycling performance curves (b and c) of S1, S2, S3 and S4 electrodes at 100 mA g^{-1}; rate performance (d) of the S2 electrode at various current densities.

Table 1 Capability comparisons of Cu–Sn alloy materials in previous works and this work

Samples	Current density	Cycle number	Capacity (mA h g^{-1})	Ref.
Copper–tin alloy	200 mA g^{-1}	15	500	26
Sn–Cu thin film	100 μA cm^{-2}	30	200	27
Cu$_6$Sn$_5$ alloy	100 mA g^{-1}	25	448	28
Cu$_6$Sn$_5$	0.13 mA cm^{-2}	10	480	29
Sn–Zn–Ni film	300 mA g^{-1}	35	444	30
Sn/Cu$_6$Sn$_5$ alloy	300 μA cm^{-2}	70	370	17
Cu$_6$Sn$_5$ alloy	50 mA g^{-1}	20	400	8
Cu$_6$Sn$_5$ alloy	100 mA g^{-1}	50	287	This work

the anodic portion, the humps of around 0.53 and 0.81 V are associated with the gradual dementalization process of Li$_2$CuSn from Li$_{3.5}$Sn and the conversion reaction of Cu$_6$Sn$_5$ from Li$_2$-CuSn referring to eqn (1)–(3),[38] in which the Cu–Sn alloy remains unaffected by the inactive Cu phase during the lithium insertion/extraction processes. The discharge–charge profiles of the S2 electrode under galvanostatic conditions for initial five cycles at 100 mA g^{-1} are illustrated in Fig. 5(b). It is worth noting that the charge–discharge curves are markedly different between the first cycle and the next four cycles, indicating that there is a potential association with the emergence of an SEI layer on the S2 electrode. Importantly, all the curves almost overlap except for the first cycle, which shows that the Cu$_6$Sn$_5$

alloy electrode exhibits excellent reversibility during the lithiation and delithiation process.

$$xLi^+ + xe^- + Cu_6Sn_5 \leftrightarrow Li_xCu_6Sn_5 \quad (1)$$

$$(10 - x)Li^+ + (10 - x)e^- + Li_xCu_6Sn_5 \leftrightarrow 5Li_2CuSn + Cu \quad (2)$$

$$3Li^+ + 3e^- + 2Li_2CuSn \leftrightarrow 2Li_{3.5}Sn + 2Cu \quad (3)$$

As depicted in Fig. 6(a), to study the dynamic behavior and investigate the Li$^+$ storage mechanism and electrochemical performance of the S2 electrode, cyclic voltammetry is conducted at various sweep rates. It is obvious that the potential of
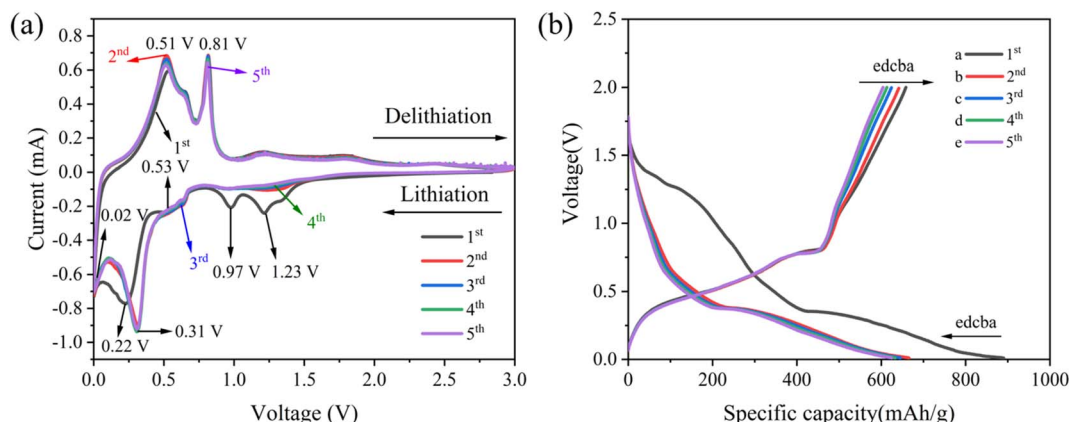
Fig. 5 CV curves (a) and galvanostatic discharge and charge profiles (b) of the S2 electrode at the first fifth cycles.
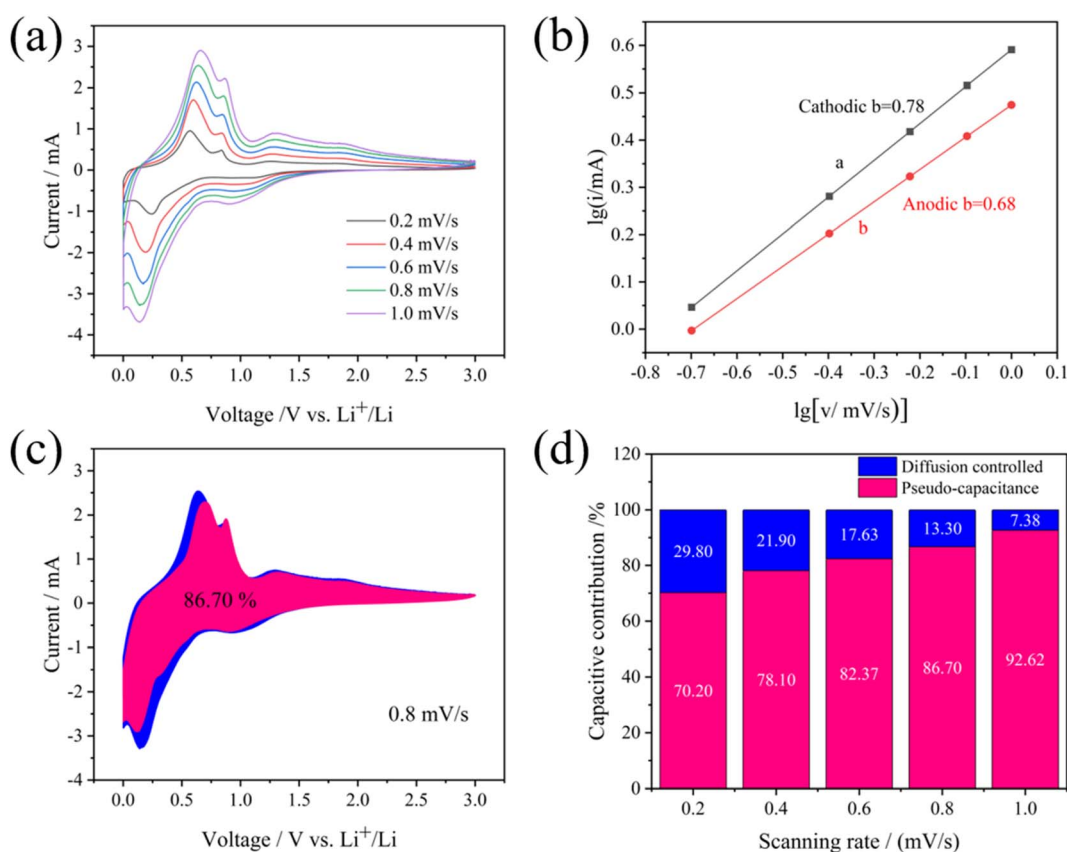

Fig. 6 CV curves at various scan rates from 0.2 to 1.0 mV s^{-1} (a), logarithmic relationship between peak currents and scan rates (b), the proportion of pseudocapacitance at 0.8 mV s^{-1} (c) and contribution ratios of pseudocapacitive and diffusion-controlled process at given scan rates (d) of the S2 electrode.

both cathodic peaks decreases along with an increase in magnitude, while the anodic peaks show a slight upward shift. The redox pseudocapacitance effect can be evaluated by utilizing the eqn (4), where a and b are constants, and the peak current (i) obeys a power-law relationship with the scan rate (v).[39] Generally, the yielded b value of 0.5 suggests a diffusion-controlled faradaic intercalation process while b value of 1.0 indicates a complete capacitive behavior via a surface faradaic

redox reaction.[40] Furthermore, when b is between 0.5 and 1, it can be estimated that capacitive and diffusive contributions are involved in the hybrid charge storage process. The fitted curves in Fig. 6(b) display b values of 0.78 and 0.68, indicating that the electrochemical characteristics are regulated by diffusion-controlled and pseudocapacitive processes, rather than a pure capacitive or faradaic process. To appraise further the influence of capacitance on the overall current response, at a certain
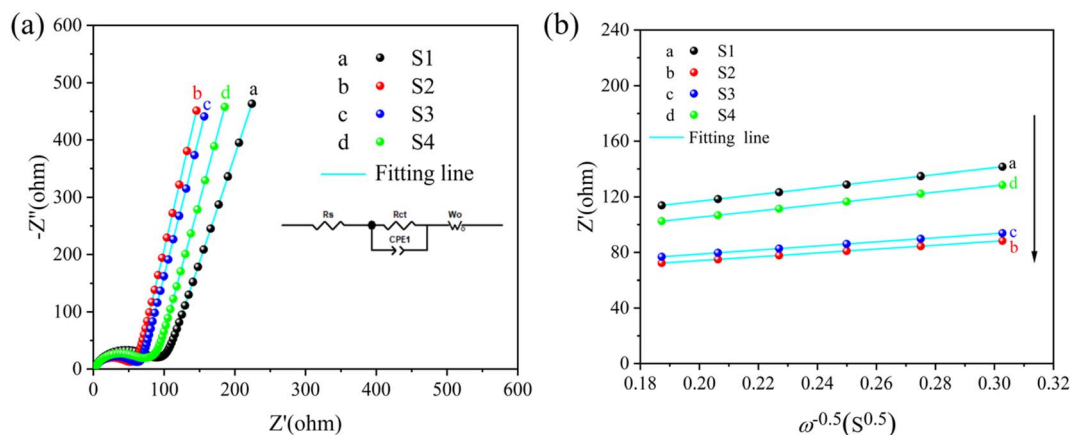
Fig. 7 Nyquist plots (a) of the as-assembled cells with S1, S2, S3, and S4 electrodes, and the corresponding fitting curves (b) of Z' vs. $\omega^{-0.5}$ in the low frequency range.

potential, the power-law relationship ($i = av^b$) is redefined as the sum of current contributions derived from diffusion-controlled processes ($k_2v^{0.5}$) and capacitive effects (k_1v) according to eqn (4) and (5).[4] Consecutively, the relative share of currents stemming from pseudocapacitors or diffusion-controlled intercalation can be calculated. Specifically, the pseudocapacitive contribution of the S2 electrode is 86.70% at 0.8 mV s^{-1} demonstrated in Fig. 6(c). As the scanning speed rises, the pseudocapacitive component resulting from the surface capacitive effect also grows, achieving a significant 86.70% contribution for the Cu_6Sn_5 alloy thin-film electrode when scanned at 0.8 mV s^{-1}. As depicted in Fig. 6(d), it is evident that the capacitive contributions relative to scan rates of 0.2, 0.4, 0.6, 0.8, and 1.0 mV s^{-1} are approximately 70.20, 78.10, 82.37, 86.70, and 92.62%, respectively. The significant capacitance contribution of the S2 electrode is primarily attributed to appropriate current density, which can enhance the homogeneous and densified surface of the S2 electrode to deliver the outstanding electrochemical performance.

$$i = av^b \qquad (4)$$

$$i(V) = k_1v + k_2v^{0.5} \qquad (5)$$

To investigate the Li$^+$ diffusion coefficient of the as-fabricated alloy sample, the EIS measurements are employed. It is important to note that the D_{Li^+} values measured by EIS tests

in a stationary state, in which by conceiving of the electrochemical process visualized as an equivalent electrical system, EIS analysis plays a pivotal role in exploring the kinetic variations of electrodes. There is a high frequency semicircle along with a low-frequency diagonal line in all impedance spectra as depicted in Fig. 7(a), in which the semicircle represents the charge-transfer resistance (R_{ct}) and the Li$^+$ diffusion character is associated with the Warburg impedance (W_o). Consequently, the curves can be fitted using equivalent circuit denoted as $[R_s(R_{ct}//CPE)W_o]$ depicted in Fig. 7(a) and the corresponding fitting parameters are detailed in Table 2. Importantly, when compared to the three other electrodes, the S2 sample exhibits a lower R_{ct} value, which can be attracted to the fact that the homogeneous and densified surface may facilitate charge transfer between the electrode and electrolyte. The curves of Z' vs. $\omega^{-0.5}$ at the low frequency range of fabricated simples at various current densities through electrodeposition are depicted in Fig. 7(b), which the Warburg factor (σ) is determined by fitting Z' linearly to $\omega^{-0.5}$ using eqn (6). Furthermore, the D_{Li^+} values of the alloy electrodes are determined using eqn (7), in which R, T, A, n, F, and C represent the gas constant, Kelvin temperature in experimental conditions, the surface area of the electrode, the number of transferred electrons per molecules during oxidation, Faraday constant and concentrations of Li$^+$, respectively, and σ is the Warburg factor. It can be seen in Table 2 that the S2 electrode has a higher D_{Li^+} value than the other three electrodes, which can be attributed to the homogeneous and densified surface can decrease the ion migration paths to increase the rate of Li$^+$ insertion and extraction. The cycling performance mentioned in Fig. 4 are consistent with the results, indicating that the properties of the Cu_6Sn_5 electrode can be significantly enhanced by controlling the current density.

$$Z' = R_s + R_{ct} + \sigma\omega^{-0.5} \qquad (6)$$

$$D_{Li^+} = \frac{R^2T^2}{2A^2n^4F^4C^2\sigma^2} \qquad (7)$$

Table 2 Relevant fitted values of the as-prepared samples at different current densities simulated from the equivalent circuits

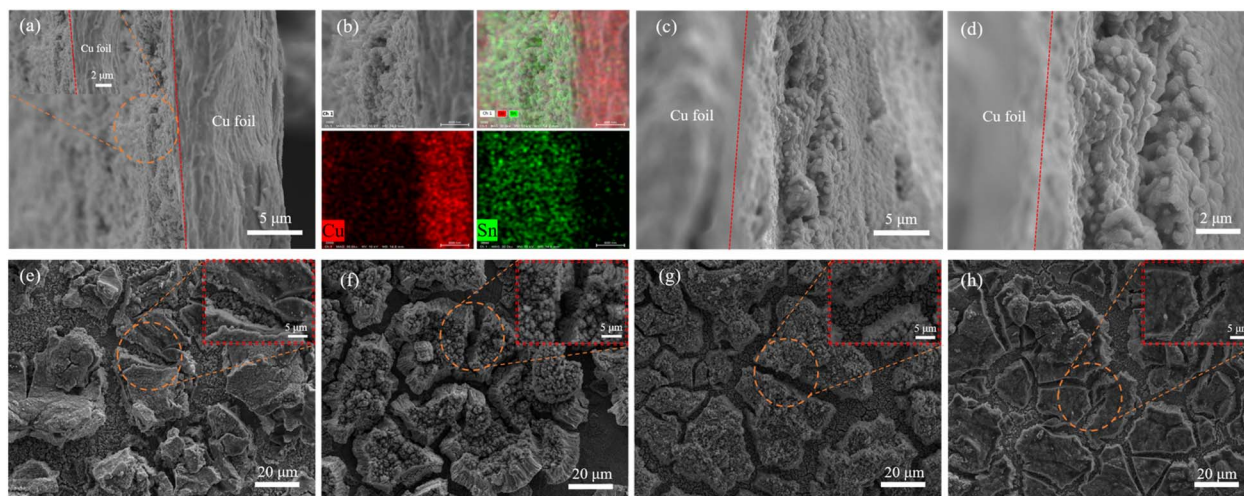| Current density (A dm^{-2})	R_{ct} (Ω)	σ (Ω cm^2 s$^{-0.5}$)	D_{Li^+} (cm^2 s^{-1})
1.0	72.96	239.13	8.936 × 10^{-16}
1.2	42.45	138.47	2.665 × 10^{-15}
1.5	51.20	147.36	2.353 × 10^{-15}
1.7	56.79	225.99	1.001 × 10^{-15}

Fig. 8 The before (a and b) and after (c and d) the circulation cross-section SEM images of S2 electrode and SEM images of S1 (e), S2 (f), S3 (g), and S4 (h) after the circulation.

The before and after the circulation cross-section SEM images of the S2 electrode and SEM images after the circulation of the S1, S2, S3, and S4 are displayed in Fig. 8. The cross-section SEM images of S2 reveal a dense structure with numerous spherical granular agglomerates and the corresponding EDS mapping images indicate that sample S2 contains copper and tin, as demonstrated in Fig. 8(a and b). From Fig. 8(c and d), it is evident that the cross-section of sample S2 after being circulated with lots of particles remains intact. Clearly, the morphology of the four electrodes after the circulation shows significant differences from those before the circulation displayed in Fig. 3, in which cracks on the surface of the disassembled electrodes are distinct. In Fig. 8(e–h), SEM images after the circulation of S1, S2, S3, and S4 reveal that the coating exfoliating from the current collector phenomenon appears to be mitigated at first and then become severe as the current density increases, in which the surface of S2 electrode maintains a consistent and intact grain with the electrodeposition current density achieving $1.2 \ A \ dm^{-2}$. The reason for these results is that the optimal current density value of $1.2 \ A \ dm^{-2}$ is advantageous in forming a uniform and dense interface, which can decrease the resistance and strengthen the contact at the interface between the current collector and the electrode, leading to significant enhancement of battery performance.

4 Conclusions

A straightforward strategy that combines electrodeposition and thermal treatment is used to fabricate Cu_6Sn_5 alloy electrodes, which include monoclinic phase η'-Cu_6Sn_5 and hexagonal phase η-Cu_6Sn_5. The investigation is focused on the impact of current density on the morphology and properties, in which dense surface of the electrode facilitated liquid electrolyte penetration and Li^+ diffusion to evidently improve the cycling stability and reversibility of reactions when the electrodeposition current density is controlled at $1.2 \ A \ dm^{-2}$. Additionally,

the optimized Cu_6Sn_5 alloy electrode showed a low charge transfer resistance and fast kinetics, which enabled excellent electrochemical lithium storage efficiency and rate capability. Therefore, a tunable strategy for fabricating Cu_6Sn_5 alloy from cyanide-free plating solution as an optimized-performance anode can be put forward to offer a promising candidate for a Sn-based anode for enhanced performance LIBs.

Data availability

The data that support the findings of this study are available from the corresponding author, [Qiuyu Zeng], upon reasonable request.

Conflicts of interest

The authors declare no competing financial interests.

Acknowledgements

References

1 Y. Li, S. Chen, W. Duan, Y. Nan, D. Ding and G. Xiao, *Energy Technol.*, 2024, **12**, 2300830.
2 L. Wang, L. Xie, Y. Song, X. Liu, H. Zhang and X. He, *Battery Energy*, 2023, **2**, 20220025.
3 S. Paul, Md. A. Rahman, Md. S. Islam, Md. R. Islam and S. Siddiqui, *Battery Energy*, 2022, **1**, 20220018.
4 R. Fang, C. Miao, H. Mou and W. Xiao, *J. Alloys Compd.*, 2020, **818**, 152884.
5 Y. Liu, P. A. Russo, L. A. Montoro and N. Pinna, *Battery Energy*, 2023, **2**, 20220037.

6 W. Jiang, W. Wang, L. Liu, H. Wang, Z. Xu, F. Li, H. Fu, H. Lv, L. Chen and Y. Kang, *J. Alloys Compd.*, 2019, **779**, 856–862.

7 Y. Xin, H. Mou, C. Miao, S. Nie, M. Wen, G. He and W. Xiao, *J. Alloys Compd.*, 2022, **922**, 166176.

8 X. Fan, F. Ke, G. Wei, L. Huang and S. Sun, *Electrochem. Solid-State Lett.*, 2008, **11**, A195.

9 G. Park, C. Lee, J. Lee, J. H. Choi, Y. Lee and S. Lee, *J. Alloys Compd.*, 2014, **588**, 534–539.

10 X. Fan, F. Ke, G. Wei, L. Huang and S. Sun, *J. Alloys Compd.*, 2009, **476**, 70–73.

11 N. Tamura, R. Ohshita, M. Fujimoto, S. Fujitani, M. Kamino and I. Yonezu, *J. Power Sources*, 2002, **107**, 48–55.

12 L. Xue, Z. Fu, Y. Yao, T. Huang and A. Yu, *Electrochim. Acta*, 2010, **55**, 7310–7314.

13 D. Zhang, C. Wang, Y. Yang, R. Guan, D. Lu, L. Gao, C. Sun and X. Bian, *J. Alloys Compd.*, 2021, **889**, 161637.

14 Z. Shen, Y. Hu, R. Chen, X. He, Y. Chen, H. Shao, X. Zhang and K. Wu, *Electrochim. Acta*, 2017, **225**, 350–357.

15 Q. Han, Z. Yi, Y. Cheng, Y. Wu and L. Wang, *RSC Adv.*, 2016, **6**, 15279–15285.

16 R. Hu, G. H. Waller, Y. Wang, Y. Chen, C. Yang, W. Zhou, M. Zhu and M. Liu, *Nano Energy*, 2015, **18**, 232–244.

17 R. Hu, M. Zeng and M. Zhu, *Electrochim. Acta*, 2009, **54**, 2843–2850.

18 X. Tan, S. Tao, L. Ran, R. Knibbe and K. Nogita, *Nano Sel.*, 2022, **3**, 1264–1276.

19 T. Sarakonsri, T. Apirattanawan, S. Tungprasurt and T. Tunkasiri, *J. Mater. Sci.*, 2006, **41**, 4749–4754.

20 X. Tan, S. D. McDonald, Q. Gu, Y. Hu, L. Wang, S. Matsumura, T. Nishimura and K. Nogita, *J. Power Sources*, 2019, **415**, 50–61.

21 J. Chen, L. Yang, S. Fang, S. Hirano and K. Tachibana, *J. Power Sources*, 2012, **199**, 341–345.

22 Z. Ni, D. Yang, Y. Wang, W. Yang, B. Deng, J. Hou, Y. Zhang, X. Li and Y. Zhang, *J. Alloys Compd.*, 2022, **906**, 164307.

23 X. Fan, Q. Zhuang, G. Wei, L. Huang, Q. Dong and S. Sun, *J. Appl. Electrochem.*, 2009, **39**, 1323–1330.

24 S. Ni, X. Lv, T. Li, X. Yang and L. Zhang, *Electrochim. Acta*, 2013, **109**, 419–425.

25 A. Kitada, N. Fukuda, T. Ichii, H. Sugimura and K. Murase, *Electrochim. Acta*, 2013, **98**, 239–243.

26 Y. Lin, J. Duh and H. Sheu, *J. Alloys Compd.*, 2011, **509**, 123–127.

27 R. Hu, Y. Zhang and M. Zhu, *Electrochim. Acta*, 2008, **53**, 3377–3385.

28 L. Yu, C. Miao, S. Nie, M. Wen, J. Wang, Y. Tan and W. Xiao, *Solid State Ionics*, 2021, **364**, 115625.

29 X. Tan, S. D. McDonald, Q. Gu, L. Wang, S. Matsumura and K. Nogita, *J. Power Sources*, 2019, **440**, 227085.

30 Z. Du, S. Zhang, F. Li, T. Jiang and Z. Bai, *Trans. Inst. Met. Finish.*, 2012, **90**, 197–202.

31 S. Nie, Y. Xin, Q. Wang, C. Liu, C. Miao, L. Yu and W. Xiao, *Int. J. Miner., Metall. Mater.*, 2023, **30**, 1171–1180.

32 A. Patil, V. Patil, D. Wook Shin, J. Choi, D. Paik and S. Yoon, *Mater. Res. Bull.*, 2008, **43**, 1913–1942.

33 P. Verma, P. Maire and P. Novák, *Electrochim. Acta*, 2010, **55**, 6332–6341.

34 L. Su, Z. Zhou and P. Shen, *J. Phys. Chem. C*, 2012, **116**, 23974–23980.

35 L. Baggetto, J. Jumas, J. Górka, C. A. Bridges and G. M. Veith, *Phys. Chem. Chem. Phys.*, 2013, **15**, 10885–10894.

36 X. F. Tan, W. Yang, K. Aso, S. Matsumura, S. D. McDonald and K. Nogita, *ACS Appl. Energy Mater.*, 2019, **3**, 141–145.

37 W. Choi, J. Y. Lee and H. S. Lim, *Electrochem. Commun.*, 2004, **6**, 816–820.

38 Z. Wang, S. Luo, F. Chen, D. Wang, Y. Liu, X. Qi, C. Shi and N. Zhao, *RSC Adv.*, 2016, **6**, 54718–54726.

39 J. Li, X. Xu, Z. Luo, C. Zhang, Y. Zuo, T. Zhang, P. Tang, M. F. Infante-Carrió, J. Arbiol, J. Llorca, J. Liu and A. Cabot, *ChemSusChem*, 2019, **12**, 1451–1458.

40 Q. Li, H. Zhang, S. Lou, Y. Qu, P. Zuo, Y. Ma, X. Cheng, C. Du, Y. Gao and G. Yin, *Ceram. Int.*, 2017, **43**, 11998–12004.